Substantially enhanced photoelectrochemical performance of TiO$_2$ nanorods/CdS nanocrystals heterojunction photoanode decorated with MoS$_2$ nanosheets

Swetha S.M. Bhat[a],[1], Sachin A. Pawar[b],[1], Darshna Potphode[c], Chang-Ki Moon[a], Jun Min Suh[a], Changyeon Kim[a], Seokhoon Choi[a], Dipali S. Patil[b], Jang-Joo Kim[a], Jae Cheol Shin[b],*, Ho Won Jang[a],*

[a] Department of Materials Science and Engineering, Research Institute of Advanced Materials, Seoul National University, Seoul 08826, Republic of Korea
[b] Department of Physics, Yeungnam University, Gyeongsan, Gyeongbuk 38541, Republic of Korea
[c] Department of Chemical Engineering, Indian Institute of Technology (IIT), Hyderabad, Kandi, Sangareddy 502285, Telangana, India

ABSTRACT

Two-dimensional (2D) MoS$_2$ nanosheets (NSs) modified 1D TiO$_2$ nanorods/0D CdS nanocrystals (NCs) heterojunction has been fabricated by all solution process as a potential anode for photoelectrochemical (PEC) water splitting applications. This heterojunction photoanode shows high photocurrent density of 3.25 mA/cm^2 at 0.9 V vs. RHE (0 V vs. Ag/AgCl) compared to the pristine TiO$_2$/CdS photoanode. The influence of MoS$_2$ NSs on PEC performance of TiO$_2$/CdS/MoS$_2$ heterojunction has been systematically investigated. We demonstrate that MoS$_2$ NSs transfer holes from CdS and facilitate further charge separation in TiO$_2$/CdS. Time resolved photo-luminescence measurement reveals increase in photoluminescence lifetime due to the presence of MoS$_2$ NSs in TiO$_2$/CdS/MoS$_2$ resulting in enhanced PEC activity. This work suggests that 1D TiO$_2$/0D CdS/2D MoS$_2$ heterojunction prototype is an interesting system where MoS$_2$ NSs can be utilized to improve charge separation in photoanodes. This study would pave the way towards designing new heterojunction functional materials for efficient PEC applications.

1. Introduction

Hydrogen fuel generation by PEC water splitting has been considered as a promising way to solve present energy and environmental issues After the discovery of TiO$_2$ photocatalysis by Fuzishima, various semiconductor materials have extensively been investigated for PEC water splitting applications [1–6]. However, low photocatalytic activity caused from high recombination rate has become a bottleneck for the industrial scale H$_2$ production. Among the numerous semiconductor architectures, the heterojunction of two or more photoelectrodes found to play significant role in improving the PEC performance [7]. As the heterojunction produces the built in electric field gradient, it helps to improve the charge carrier transfer rate at the electrode – electrolyte interface [8]. TiO$_2$, a wide band gap semiconductor stands as a benchmark photocatalyst owing to its long minority diffusion length, low toxicity, high photostability and wide abundance [9]. In order to improve the overall efficiency of TiO$_2$ photocatalyst several approaches

have been adopted such as crystal facet engineering, doping and constructing heterojunction with suitable semiconductors [9–11]. Doping of TiO$_2$ with metal or nonmetal usually leads to the trapped states which serve as a centre for recombination of electron-hole pair [10]. Fabrication of TiO$_2$ heterojunction photoanode is advantageous as it achieves superior charge transfer property while simultaneously extending the light absorption edge [12].

Wide band gap materials are usually heterojunctioned with narrow band gap semiconductors in order to reduce the recombination rate and also to extend the light absorption window [13,14]. CdS, a direct band gap semiconductor which can absorb visible light up to 520 nm wavelength is a potential candidate as it possesses low work function [15,16]. Since the conduction band edge has more negative potential than the hydrogen reduction potential, CdS NCs, 0D material, have been vastly used for H$_2$ evolution reaction [17]. Several studies reported the fabrication of TiO$_2$/CdS for solar water splitting applications [18,19]. CdS can easily be synthesized by several solution methods such

as successive ionic layer adsorption and reaction (SILAR), chemical bath deposition (CBD), electrochemical deposition and hydrothermal techniques [20,21].

MoS_2, a two-dimensional layered material, has extensively been used in optoelectronic devices, photodetectors, and photodiodes. MoS_2 has been recognized as a promising hydrogen evolving semiconductor in 2H phase with the band gap of 1.2 eV. Numerous efforts have been focused on developing MoS_2 for hydrogen evolution reaction due its unique molecular and electronic structure. It is worthwhile to note that MoS_2 has been demonstrated as a co-catalyst which shows better activity than the noble metal Pt. Recent reports prove that MoS_2 can also be used as a photoanode for water oxidation [22]. CdS/MoS_2 heterojunctions have emerged as promising water splitting photocatalysts [23–26]. Multilayered MoS_2 which shows n-type conductivity was composited with CdS to form type I heterojunctions [26,27]. From the recent studies it can be inferred that CdS/MoS_2 has been extensively investigated especially as hydrogen evolution photocatalysts [26,28]. However, fabrication of CdS/MoS_2 photelectrodes have received very less attention though both materials possess sufficient oxidation potential for oxygen evolution reaction. It is well recognized that one dimensionally ordered nanorods arrays of TiO_2 offer improved facet exposure and directional diffusion pathways for carriers which improve the charge separation. Therefore, construction of double heterojunction of $TiO_2/CdS/MoS_2$ would be promising photoelectrode materials for PEC water splitting applications.

In this present work, we report the fabrication of $TiO_2/CdS/MoS_2$ with ZnS from all solution process. This is the first demonstration of $TiO_2/CdS/MoS_2$ heterojunction photoanode exhibiting remarkably high photocurrent density. ZnS is known to inhibit the trap states in CdS layer, therefore, ZnS layer has been coated on the photoelectrodes to enhance the photostability [27]. In this $TiO_2/CdS/MoS_2$ prototype, MoS_2 acts as a hole capturer which accelerates the fast transfer of holes into electrolyte while CdS serves as a light sensitizer to harvest wide range of solar spectrum. TiO_2 nanorods (NRs) help for improved electrical conductivity which carry electrons to the fluorine doped tin oxide (FTO) substrate. $TiO_2/CdS/MoS_2$ photoelectrode shows higher photo activity compared to TiO_2/CdS heterojunction. Enhanced PEC activity can be attributed to MoS_2 NSs which speed up the charge transfer between the photoelectrode and electrolyte. This systematic study helps to develop varieties of heterojunctions of the light sensitizing semiconductor with the wide band gap materials to achieve better PEC performance.

2. Experimental

2.1. Synthesis of TiO_2 nanorods

TiO_2 nanorods (NRs) were synthesized on FTO substrate by hydrothermal technique. In a typical procedure, 0.4 mL of titanium butoxide (Sigma Aldrich, purity ≥ 97%) was dissolved in a solution of hydrochloric acid (26 mL, Daejung, purity ≥ 97%) and distilled water (24 mL). The resultant solution was transferred to a Teflon containing cleaned FTO which was placed at the bottom. The autoclave was heated at 200 °C for 3 h. After the synthesis, autoclave was cooled to room temperature naturally. TiO_2 grown FTO substrate was washed extensively with distilled water and dried in ambient air. FTO substrate was annealed at 400 °C for 3 h in ambient atmosphere to obtain the crystalline rutile TiO_2.

2.2. Synthesis of TiO_2/CdS

CdS nanocrystals (NCs) are coated on TiO_2 NRs by CBD technique. A CdS solution was prepared by mixing 1.5 mM cadmium nitrate (Cd$(NO_3)_2$, (Sigma Aldrich, purity ≥ 98%) and 1.5 mM sodium sulfide nonahydrate ($Na_2S.9H_2O$, Sigma Aldrich, purity ≥ 98%) in distilled water. The TiO_2 NRs film was dipped in a CdS precursor solution

containing glass vial and put in the oven after sealing it for 5 min at 85 °C. The reaction time has been from 5, 15, 30 and 60 min and the optimized reaction time was 30 min. Once the reaction was complete, the TiO_2 NRs/CdS sample was rinsed thoroughly using distilled water and allowed to dry naturally.

2.3. MoS_2 nanosheets (NSs) synthesis

In a typical process, 500 mg of MoS_2 (< 2 μm size) was dispersed in 50 mL of DMF (N, N-dimethyl formamide) for 8 h by probe sonication. During sonication, ice was used to maintain the temperature of DMF less than room temperature. Then the suspension was allowed to settle for 12 h without disturbance. Further 70% of the supernatant solution was decanted and refluxed at 140 °C for 6 h with vigorous stirring to obtain exfoliated MoS_2 as a yellow color liquid. Then the suspension was centrifuged for 1 h at 8000 rpm to settle residue of bigger size particles. The yellow color liquid then separated from residue and solvent was evaporated by rotavapor under vacuum to yield blackish brown solid. The obtained MoS_2 NSs further dried in a vacuum oven for 12 h at 60 °C.

2.4. Synthesis of $TiO_2/CdS/MoS_2$

The MoS_2 NSs were prepared in a dimethyl formamide (DMF) solution by exfoliating the bulk MoS_2 powder (Sigma Aldrich, purity ≥ 99%). The detailed exfoliation protocol is mentioned as above. The MoS_2 NSs are re-dispersed in ethanol solution. CBD technique was employed for MoS_2 deposition on TiO_2 NRs/CdS. While depositing different layers of MoS_2, 0.5, 1, 1.5 and 2 mL of MoS_2 NSs dispersed in ethanol solution was used along with CdS CBD solution. The MoS_2 NSs were decorated in-situ on TiO_2 NRs/CdS during CBD. Here, 1.5 mL MoS_2 NSs solution was the optimized quantity used for further analysis.

2.5. ZnS passivation layer

In order to deposit ZnS passivating layer on optimized TiO_2/CdS and TiO_2 NRs/CdS/MoS_2 heterojunction, successive ionic layer adsorption and reaction (SILAR) technique is employed. Hereafter, ZnS coated photoanodes are referred to as TiO_2/CdS and $TiO_2/CdS/MoS_2$ unless otherwise stated.

Four SILAR cycles have been employed to coat ZnS using an aqueous solution containing 0.1 M Zn $(NO_3)_2$ (Sigma Aldrich, purity ≥ 98%) and 0.1 M $Na_2S.9H_2O$ having Zn^{2+} and S^{2-} sources, respectively. Distilled water was used for rinsing the photoanode in the above SILAR sequence.

3. Characterizations of electrodes

The phase of the samples was confirmed by PANalytical diffractometer equipped with Cu Kα source. The morphology of the TiO_2 NRs/CdS/MoS_2 phototoanodes were characterized using a field-emission SEM (SU-70, Hitachi), with an acceleration voltage of 5 kV and working distance of 8 mm by field emission SEM (SU-Hitachi). The transmission electron microscope (Tecnai G2 F20, FEI Company) analysis were carried out at an accelerating voltage of 200 kV, which was equipped with high-angle annular dark-field image (HADDF), scanning TEM (STEM), and energy dispersive spectroscopy (EDS). UV–vis absorbance spectra were obtained by JASCO UV–vis spectrometer. TR- PL spectra were measured using a pulsed nitrogen laser (Usho Optical Systems Co. Ltd, λ = 337 nm), a pulse generator (Agilent 8114A), and a streak camera (C4334, Hamamatsu Photonics).

3.1. Photoelectrochemical (PEC) characterization

PEC performances of phototoanodes were measured with a typical three electrode configuration using Ivium potentiostat with Ag/AgCl as

reference electrode and Pt plate as a counter electrode. Aqueous solution of 0.35 M Na_2SO_3 and 0.25 M Na_2S was used as electrolyte for all the measurements. 0.35 M Na_2SO_4 and 0.25 M Na_2S aqueous electrolyte has been used in order to measure the LSV of the photoelectrodes in the absence of hole scavenger. The light intensity of solar simulator with an AM 1.5 G filter was calibrated to 1 Sun (100 mW/cm²) using a reference cell. Linear sweep voltammogram (LSV) measurements were carried out by sweeping in the anodic direction with scan rate of 20 mV/S. Incident photon to current conversion efficiency (IPCE) values were measured at 0 V vs Ag/AgCl (0.9 V vs. RHE) using light source with monochromator. EIS was conducted at 0 V vs Ag/AgCl (0.9 V vs. RHE) with the frequency range 10 mHz–1000 Hz and the obtained plots were fitted using ZSimpWin suite. Gas chromatography measurement system (Agilent GC 7890B) equipped with a thermal conductivity detector and a micro-packed column (ShinCarbon ST 100/120) was used to measure the H_2 evolution.

4. Results and discussion

TiO_2 NRs were grown on FTO substrate by adopting previously reported work [28]. Further, TiO_2 NRs were coated with CdS, MoS_2, and ZnS by all solution process, the details of which are given in the Supporting Information. The schematic illustration of the synthesis of heteorjunciton photoanode has been presented in the Fig. 1(a).

The uniform coverage of TiO_2 NRs by CdS NCs and MoS_2 NSs can be evidenced through the visible surface roughness on TiO_2 NRs. This is evident of TiO_2/CdS/MoS_2 heterojunction formation which is believed to be favourable for enhanced absorption of solar spectrum in the visible region and thereby leading to higher PEC performance compared to pristine TiO_2 NRs. It is well recognized that ZnS has been employed to inhibit the photocorroison and electron passivation. To prevent the photocorrosion of CdS, ZnS has been deposited by SILAR method. Therefore, it should be noted that the all the photoanodes consisting of CdS are coated with ZnS unless otherwise it is specified. Cheng et al. reported similar surface morphological features for heterojunction of TiO_2 nanotubes decorated with CdS/CdSe/ZnS [29]. A typical FESEM images of TiO_2 NRs on FTO is shown in Fig. S1(a), (b). It can be observed from the SEM images that the length of TiO_2 NRs was around 4 μm with 170 nm in diameter (Fig. 1(d)). The morphology of TiO_2 NRs with faceted apex and smooth side surfaces which are very inherent to hydrothermal technique. CdS has been coated on TiO_2 NRs by CBD method. Fig. S1c–d shows the FESEM images of TiO_2 NRs after CdS NCs coating at different magnifications. These images indicate that CdS NCs have been uniformly decorated which is utmost important for extending the ability of TiO_2 to harness visible solar spectrum [30]. In order to assess the uniform and optimum coverage of CdS NCs over TiO_2 NRs we monitored the CdS solution concentrations from 0.25 mM to 2 mM in the CBD process. The corresponding FESEM images are shown in Fig. S2; it is observed that the optimum coverage of CdS NCs takes place for 1.5 mM CdS solution concentration. Further increase in the CdS solution lead to the agglomeration of CdS NCs over TiO_2 NRs (Fig. S2). After MoS_2 NSs coating on TiO_2 NRs, usually a smooth thin film could be observed from TiO_2/MoS_2 sample. However, there wasn't any significant distinguishable surface morphology of TiO_2/MoS_2 compared to TiO_2/CdS NCs (Fig. S2(e)–(f)). It could be due to the formation of very thin inseparable MoS_2 NSs over TiO_2 NRs. The cross-sectional SEM images of sample TiO_2/CdS/MoS_2 are depicted in Fig. 1(d) and (e) at lower and higher magnifications which show that the relatively smooth TiO_2 NRs are turned into rougher and uneven surfaces. This discloses that the CdS NCs and MoS_2 NSs have enclosed the entire surfaces of TiO_2 NRs. It should be noted that such heterojunction formation is highly beneficial for excellent PEC activity since rutile TiO_2 has limitation to harvest visible light due to wide band gap. To extend the activity of photoanode into the visible light region NCs of small band gap semiconductors have been used as sensitizers [31]. Further, CdS can initiate wider light absorption range than pristine TiO_2

and has high conduction band edge in comparison to pristine TiO_2 and a higher electron injection efficiency. This can be coupled with hole scavenging MoS_2 to form a photoanode with superior PEC performance.

Structural and morphological features were further analysed by high resolution transmission electron microscope (HRTEM) and high-angle annular dark-field image-scanning TEM (HAADF-STEM). Fig. 2(a) and (b) are TEM and HRTEM images of sample TiO_2/CdS/MoS_2, respectively. TEM image shows TiO_2 NRs are uniformly covered by CdS NCs and MoS_2 NSs. We found the sizes of CdS nanocrystals and MoS_2 nanosheets to be ˜15–30 nm and ˜10–20 nm from TEM analysis of pristine CdS and MoS_2 samples, respectively (Fig. S3). The CdS NCs were visible as dots on the exterior of TiO_2 NRs which are adhered to the NRs and the MoS_2 NSs have covered them all. The HRTEM image of TiO_2/CdS/MoS_2 heterojunction decorated by ZnS NPs shows high crystallinity for TiO_2, CdS, MoS_2. The TiO_2 NR with lattice spacing of 0.32 nm suggests its high orientation with respect to the FTO substrate surface and is ascribed to lattice plane (110). CdS NCs decorated on TiO_2 NRs have d-spacing around 0.22 nm corresponding to (200) crystal plane of hexagonal CdS. Similarly, interplanar distance of 0.23 nm corresponding to (104) crystal plane is due to presence of MoS_2.

It should be noted that the heterojunction formation took place without noticeable contamination from organic solvent residues which could have posed recombination losses significantly [32]. STEM and corresponding STEM-EDS elemental mapping of sample TiO_2/CdS/MoS_2 have been carried out to further confirm that the CdS/MoS_2/ZnS covers the exterior of TiO_2 NRs surface. Fig. 2(d)–(i) shows the distribution of Cd, S, Mo and Zn elements on TiO_2 NRs. These results corroborate the formation of heterojunction TiO_2/CdS/MoS_2.

The formation of the pure phase and crystal structure of TiO_2 NRs/CdS/MoS_2 was confirmed by X-ray diffraction (XRD) as shown in Fig. 2(c). All the crystallographic planes for TiO_2, CdS and MoS_2 are in accordance with the JCPDS data files. The diffraction peaks at 2θ = 14.48, 29.20, 34.16, 41.12, 48.05, 58.35 and 60.76° correspond to (003), (006), (012), (104), (018), (110) and (113) crystal planes which are attributed to rhombohedral crystal structure of MoS_2 (JCPDS card 01-086-2308) [33]. Similarly, the diffraction peaks at 26.45, 30.64, 43.88, 51.97, 54.57, 63.80 and 70.33° belong to (111), (200), (220), (311), (222), (400) and (331) crystal planes of hexagonal CdS system (JCPDS card 03-065-2887) [34]. Besides these peaks, the diffraction peaks located at 27.96, 39.96, 44.92 and 68.58° assigned to (110), (200), (210) and (221) crystal planes of tetragonal rutile TiO_2 crystal structure (JCPDS card 01-082-0514) [35]. XRD of pristine TiO_2 and TiO_2/CdS are presented in the Supporting Information (Fig. S4) which confirms the presence of rutile TiO_2 and hexagonal CdS, respectively. Apart from the peaks mentioned above, the peaks marked as # are from the substrate FTO. There were no peaks of impurities observed affirming the phase pure samples. ZnS being too thin in nature was not observed in XRD however its presence was confirmed by XPS measurements (Fig. S5).

The elemental compositions and chemical states of TiO_2/CdS and TiO_2/CdS/MoS_2 were determined by XPS measurements as shown in Fig. 3(a)–(d). High resolution XPS spectrum of Ti 2p for sample TiO_2/CdS is shown in the lower panel of Fig. 3a while that of TiO_2/CdS/MoS_2 is shown in the upper panel. The peaks centered at 457.82 and 463.38 eV are due to Ti $2p_{3/2}$ and Ti $2p_{1/2}$ states of element Ti respectively confirming presence of Ti^{4+} cation in TiO_2 for TiO_2/CdS sample [35]. While, very weak Ti 2p signal was observed for the sample TiO_2/CdS/MoS_2 (shown in upper panel of Fig. 3(a)). This is due to successive layer formation on TiO_2 NRs lead to reduced intensity of the peaks significantly. Similar behavior was observed in core-shell structure of IrO_2/CdSe/CdS/TiO_2 reported by Sun et al., where there was hardly any detectable signal from TiO_2 modified NRs [36]. The lower panel in Fig. 3(b) is high resolution XPS of O 1s spectra for sample TiO_2/CdS with the peak centred at 529.38 eV corresponding to O 1s state due to Ti−O bonding. The O 1s peak is located at 529.58 eV in
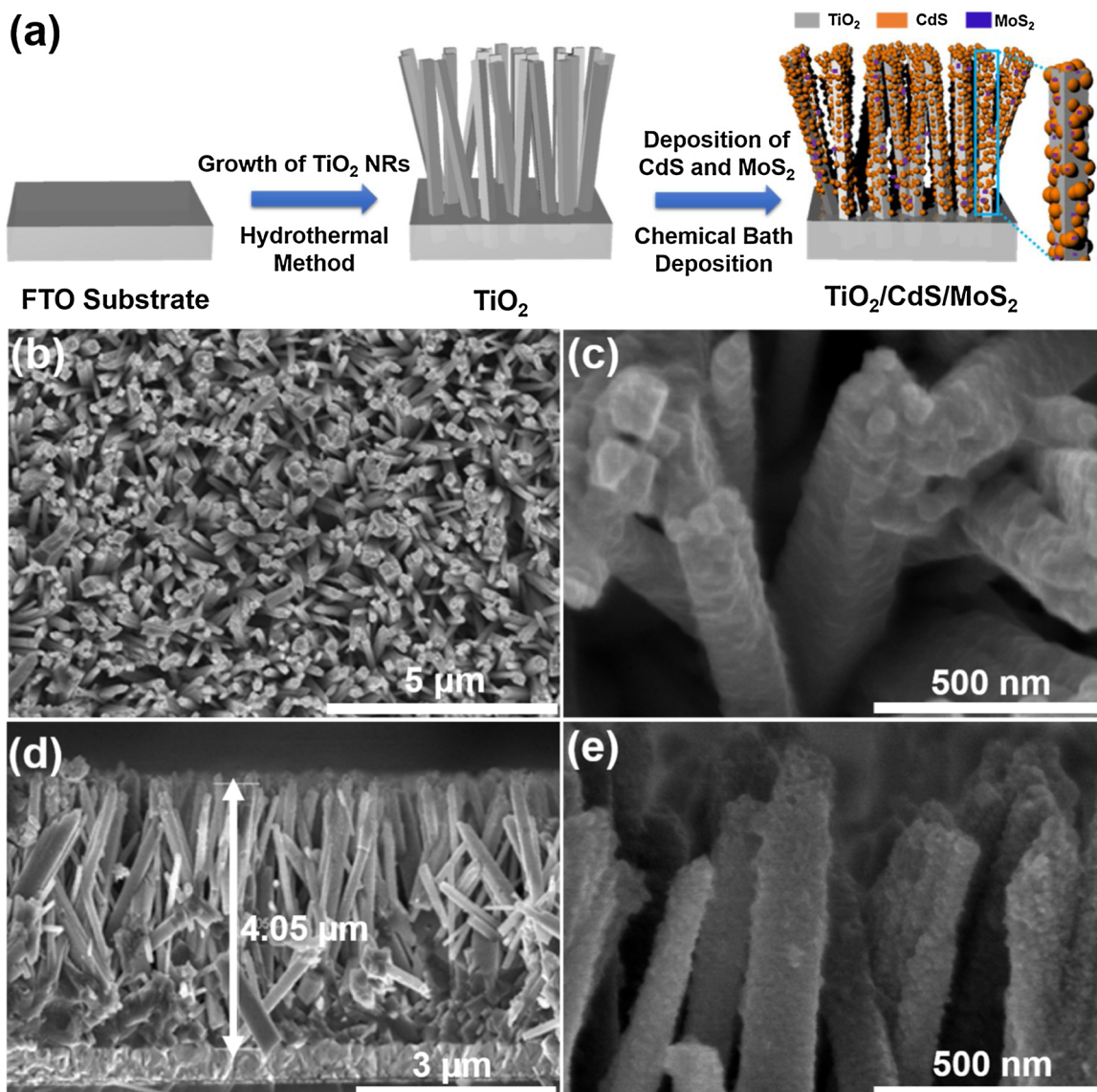
Fig. 1. (a) Schematic illustration of TiO$_2$/CdS/MoS$_2$ synthesis. (b, c) Scanning electron microscopy (SEM) top images of TiO$_2$/CdS/MoS$_2$ on FTO substrate at (b) low and (c) high magnification. (d, e) SEM cross-section images of TiO$_2$/CdS/MoS$_2$ on FTO substrate at low and (e) high magnification.

sample TiO$_2$/CdS/MoS$_2$ in the upper panel indicating slight higher values in binding energy which could be due to Cd–O and Mo–O bonding. Further, the peaks located at 530.98 and 531.08 eV in O 1s of TiO$_2$/CdS and TiO$_2$/CdS/MoS$_2$, respectively indicates presence of oxygen vacancy and adsorbed water molecules [37]. The spectra in Fig. 3(c) in upper and lower panel are due to Cd 3d in TiO$_2$/CdS/MoS$_2$ and TiO$_2$/CdS, respectively. It shows two different peaks Cd 3d$_{5/2}$ and Cd 3d$_{3/2}$ with binding energies 404.38, 411.08, 405.08 and 411.78 eV for TiO$_2$/CdS and TiO$_2$/CdS/MoS$_2$, respectively.

It should be noted that the peak separation distance in both the cases is 6.7 eV, confirming Cd^{2+} cations in CdS crystal structure [38]. The shift in binding energy for TiO$_2$/CdS/MoS$_2$ sample indicates the strong interaction between CdS and TiO$_2$ [39]. S 2p high resolution spectra consist of S 2p$_{3/2}$ and S 2p$_{1/2}$ as shown in Fig. 3(e) with the binding energies 160.75, 161.88, 161.67 and 162.78 eV, in samples TiO$_2$/CdS and TiO$_2$/CdS/MoS$_2$, respectively. It indicates that the valence state of element S is −2 [40]. Similarly, high resolution XPS spectra of Mo 3d are shown in Fig. 3d consisting of two distinct peaks of Mo 3d$_{5/2}$ and Mo 3d$_{3/2}$ orbitals located at 229.40 and 232.50 eV, respectively confirming the core levels of the Mo^{4+} cations in MoS$_2$ [41]. There appear a shoulder peak at 226.75 eV which corresponds to S (2 s).

The binding energy values for Mo 3d$_{5/2}$ and Mo 3d$_{3/2}$ were consistent with the observed one reported in the literature [42–45]. The existence of Mo^{6+} will lead to the peaks at 233.1 and 235.9 eV due to Mo 3d orbitals. However, in this case, the Mo 3d orbitals are located at different binding energies hence there is no formation of Mo^{6+} [23]. It should be noted that the energy separation between Mo 3d$_{5/2}$ and Mo 3d$_{3/2}$ is 3.11 eV (< 3.3 eV) and is indicative of presence of MoS$_2$. Moreover, the energy separation in S 2p$_{3/2}$ and S 2p$_{1/2}$ peaks in TiO$_2$/CdS/MoS$_2$ sample is ≤ 1.4 eV (1.1 eV) which is evident of formation of MoS$_2$ and not that of amorphous MoS$_3$ (≥ 1.4 eV) [46]. High resolution XPS of pristine TiO$_2$ and Zn 2p core levels is presented in Fig. S5, confirming the presence of Ti, O and Zn elements. The above XPS results confirm the successful heterojunction formation of TiO$_2$/CdS/MoS$_2$ fabricated by all solution processes.

PEC properties of TiO$_2$, TiO$_2$/CdS and TiO$_2$/CdS/MoS$_2$ were investigated in three electrode configuration with Pt plate as counter electrode and Ag/AgCl as reference electrode. Fig. 4(a) represents linear sweep voltammograms (LSV) of TiO$_2$, TiO$_2$/CdS and TiO$_2$/CdS/MoS$_2$ under chopped illumination. TiO$_2$ and TiO$_2$/CdS show photocurrent of ~1.01 and 1.95 mA/cm^2, respectively. While TiO$_2$/CdS/MoS$_2$ exhibits the maximum photocurrent density of ~3.45 mA/cm^2 at 0.9 V
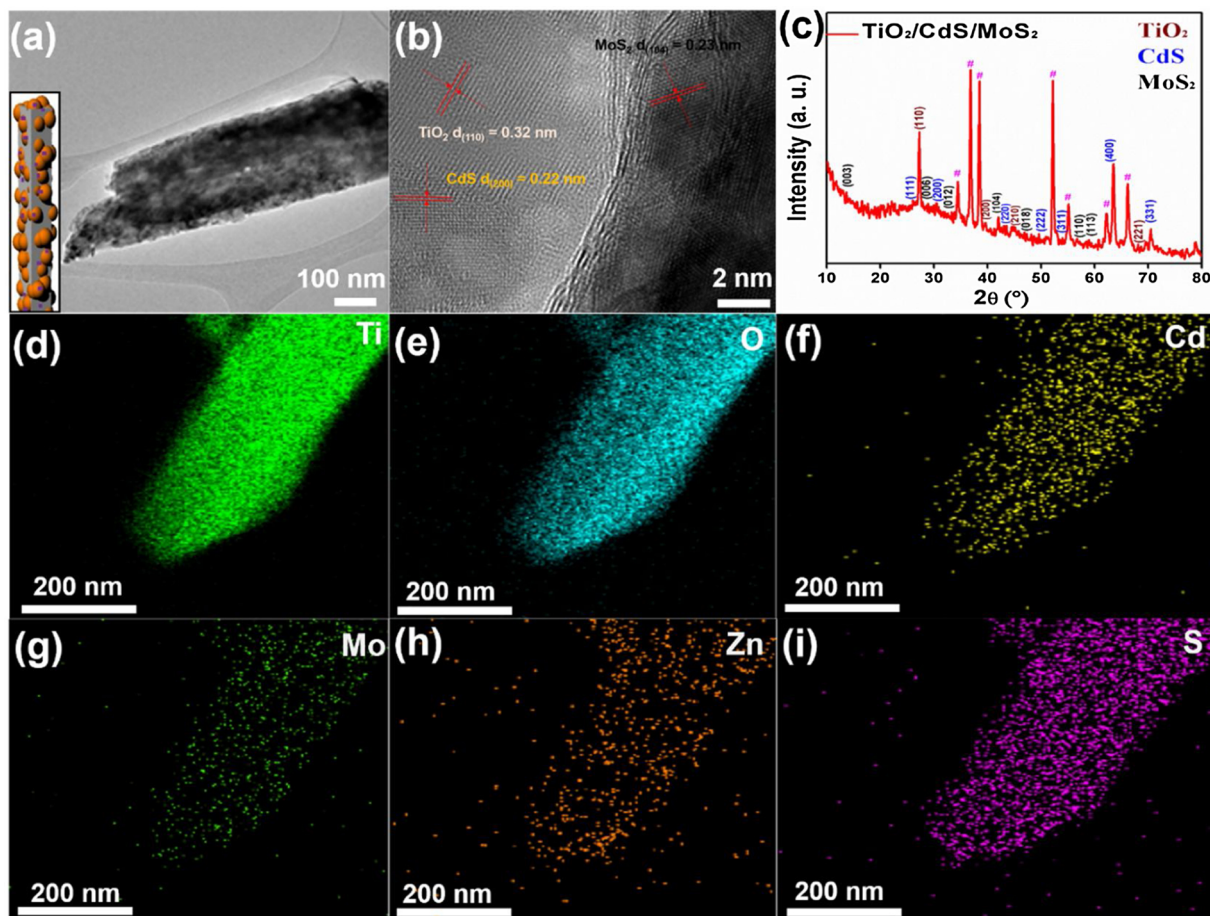
Fig. 2. (a) Transmission electron microscope (TEM) image of $TiO_2/CdS/MoS_2$. Inset shows schematic illustration of $TiO_2/CdS/MoS_2$. (b) High resolution TEM (HRTEM) with lattice fringes of $TiO_2/CdS/MoS_2$. (c) X-ray diffraction pattern of $TiO_2/CdS/MoS_2$ (d)-(i) HAADF-STEM elemental mapping of sample $TiO_2/CdS/MoS_2$ with ZnS passivation layer showing the distribution of Ti, O, Cd, Mo, Zn, and S.
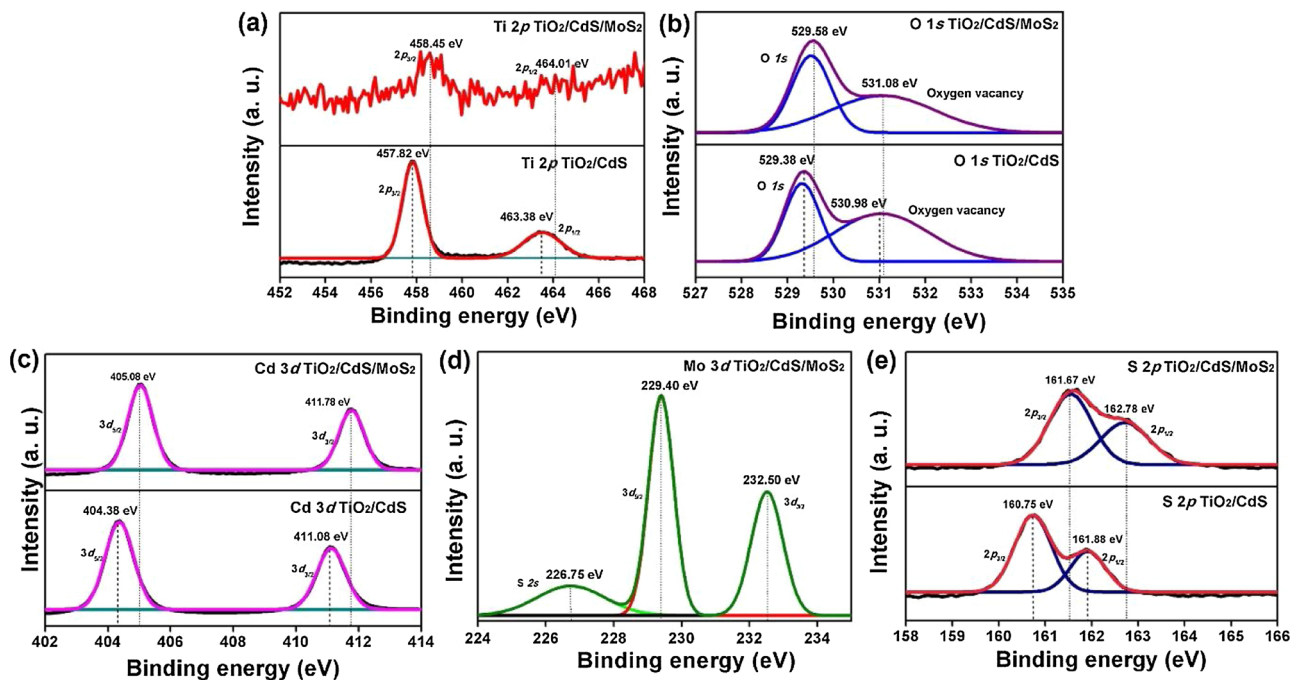

Fig. 3. XPS of TiO_2/CdS and $TiO_2/CdS/MoS_2$: High resolution scans of (a) Ti 2p, (b) O 1s, (c) Cd 3d, (d) Mo 3d, and (e) S 2p.
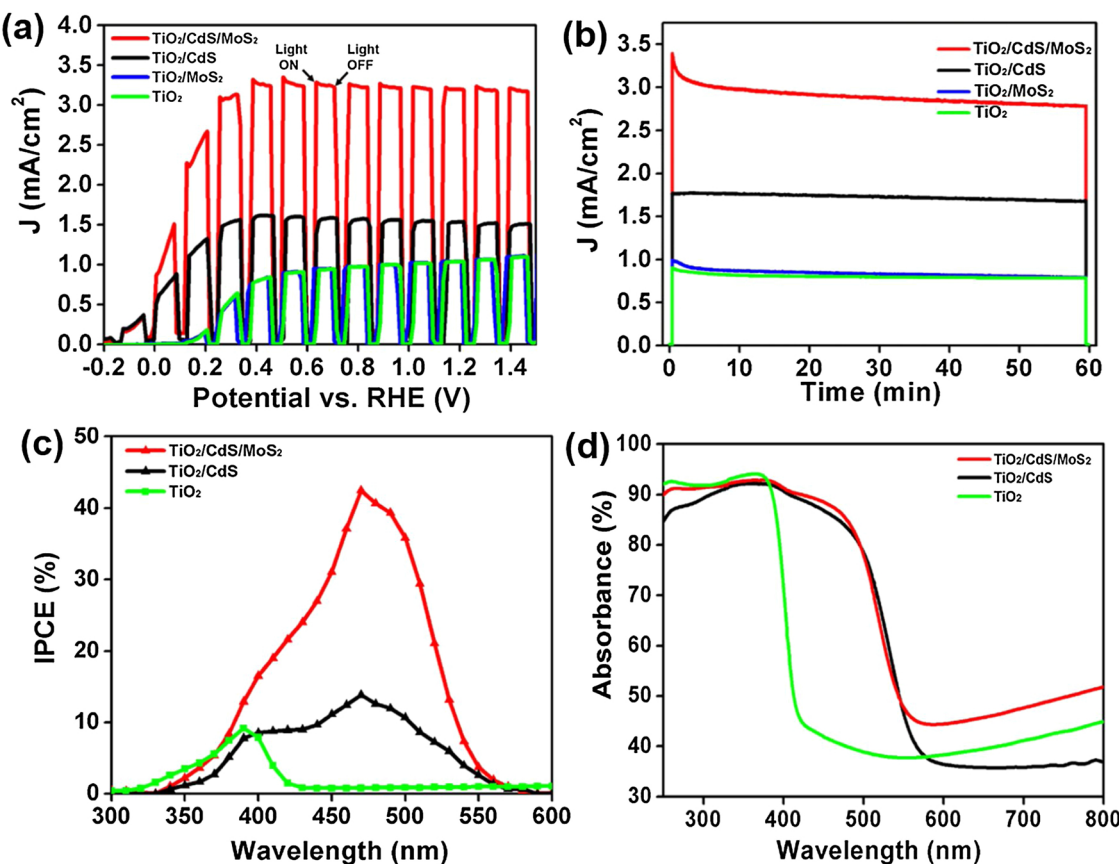
Fig. 4. (a) LSV of $TiO_2/CdS/MoS_2$, TiO_2/CdS, TiO_2/MoS_2 and TiO_2 measured using a three-electrode configuration under chopped illumination. (b) Stability measurements of the $TiO_2/CdS/MoS_2$, TiO_2/CdS, TiO_2/MoS_2 and TiO_2 photoanodes at 0.9 V vs. RHE (0 V vs. Ag/AgCl) under one sun illumination. (c) Incident photon to current conversion efficiency (IPCE) of $TiO_2/CdS/MoS_2$, TiO_2/CdS and TiO_2 measured at 0.9 V vs. RHE (0 V vs. Ag/AgCl) in aqueous 0.35 M Na_2SO_3 and 0.25 M Na_2S electrolyte (pH 12). (d) UV–vis absorbance spectra of $TiO_2/CdS/MoS_2$, TiO_2/CdS, and TiO_2 photoelectrodes.

vs. RHE (0 V vs. Ag/AgCl). In contrast to $TiO_2/CdS/MoS_2$, there was no enhancement in the photoactivity of TiO_2/MoS_2 heterojunction compared to pristine TiO_2 indicating that it failed to establish the intimate contact between TiO_2 and MoS_2, consequently, charge transfer was ineffective. It is noteworthy that TiO_2 onset potential is found to be ~0.07 V vs. RHE which has been shifted to -0.09 V for TiO_2/CdS. While $TiO_2/CdS/MoS_2$ shows the onset potential is similar to TiO_2/CdS, the steep rise in the photocurrent density at the lower external bias can be seen compared to TiO_2/CdS. This negative shift in the onset potential is due to CdS as it possesses the low conduction band potential. The LSV measurement was carried out in the absence of the hole scavenger and is presented in Fig. S6. It is found that the $TiO_2/CdS/MoS_2$ shows a descent photocurrent density of 2.25 mA/cm^2 at 0.9 V vs. RHE (0 V vs. Ag/AgCl). The dark current for all the photoelectrodes are presented in Fig. S7(a). Further, the transient phototocurrent has been measured to probe the charge dynamics of the PEC performance driven by $TiO_2/CdS/MoS_2$ photoanode (Fig. 4(a)).

Usually, the initial spike in the photocurrent corresponds to the band bending which arises from hole drifting to the surface. As it can be seen from the Fig. 4(a), the spike for $TiO_2/CdS/MoS_2$ heterojunction is significant compared to TiO_2/CdS and prisitine TiO_2. It is unlikely that surface passivation of MoS_2 is negligible indicating that improved PEC performance is due to the charge separation at the interface.

Increase in the photocurrent density for TiO_2/CdS is observed which is due to the formation of the type II heterojunction between CdS and TiO_2 as reported previously [47–49]. Further enhancement in the photocurrent density for $TiO_2/CdS/MoS_2$ clearly indicates the vital role of MoS_2. Chronoamperometric measurements have been carried out to evaluate the stability of $TiO_2/CdS/MoS_2$ as shown in Fig. 4(b). The

stability of the chalcogenide compounds is a very important issue as they are vulnerable for photocorrosion. Photocorrosion of CdS arises from the oxidation of sulfide ions from holes or hydroxyl radicals resulting in the dissolution of Cd ion into the electrolyte. Immense efforts have been dedicated to tackle the photochemical instability of CdS by coupling with wide band gap semiconductor. It is very well known from the literature that the ZnS, a wide band gap semiconductor, has been used as a passivation layer to avoid the photocorrosion of CdS by passivating surface deep traps [50]. ZnS is found to be the stable photocatalyst among sulfide semiconductors. This is mainly due to the large negative potential of the conduction band minimum, consequently, it facilitates the rapid photo generation and separation of charge carriers occur at the ZnS surface. As a result, the oxidation of S^{2-} on ZnS surface is drastically reduced. Thin layer of ZnS has been coated on $TiO_2/CdS/MoS_2$ in order to inhibit the photocorrosion of CdS. It is also noteworthy that the electrolyte S^{2-}/SO_3^{2-} which scavenges the holes to prevent oxidative photocorrosion has been used in order to avoid further degradation. The long term stability of $TiO_2/CdS/MoS_2$ photoanode has also been tested for 600 min and found that around 77% of the initial photocurrent is retained even after 600 min of continuous illumination. The slight difference in the photocurrent density of $TiO_2/CdS/MoS_2$ in Figs. 4(b) and S9 for the initial 60 min (0.2 mA/cm^2) is negligible.

As there was insignificant difference between the pristine TiO_2 and TiO_2/MoS_2 in terms of PEC performances (Figs. 4(a–b) and S7b), we have carried out further measurements only for TiO_2, TiO_2/CdS and $TiO_2/CdS/MoS_2$.

Fig. S8 shows the LSV of $TiO_2/CdS/MoS_2$ without ZnS and $TiO_2/CdS/MoS_2$ with ZnS. The photocurrent decays rapidly with subsequent LSV scans for $TiO_2/CdS/MoS_2$ without ZnS. In contrast, the stable

photocurrent is maintained for ZnS loaded $TiO_2/CdS/MoS_2$ photoanode. It reveals that ZnS is effective in protecting CdS from undergoing photocorrosion. Stability of $TiO_2/CdS/MoS_2$ photoanode was investigated for 60 min and observed that photocurrent decay was negligible. It is noteworthy that the spike is observed when the light is switched on for $TiO_2/CdS/MoS_2$. Slight decay of the photocurrent indicates that the fraction of the holes generated at the interface of electrode/electrolyte either it reaches back to the surface of the semiconductor or being captured by the electron in conduction band instead of recombining with electrons from the electrolyte. However, with increase in the illumination time, $TiO_2/CdS/MoS_2$ achieves stable photocurrent. It suggests that after the excess holes have undergone recombination, the photogenerated carriers reach equilibrium to give constant photocurrent as it can be seen in Fig. 4(b) [23]. IPCE was measured for TiO_2, TiO_2/CdS and $TiO_2/CdS/MoS_2$ at 0 V vs Ag/AgCl (0.9 V vs. RHE) in three electrode configuration using aqueous Na_2SO_3 and Na_2S electrolyte. TiO_2/CdS exhibits ~15% at 475 nm, on other hand, deposition of MoS_2 on TiO_2/CdS shows substantial enhancement in IPCE exhibiting 45% of IPCE at 475 nm. In contrast to wide band gap TiO_2 NRs which showed maximum of ~10% IPCE at 390 nm, TiO_2/CdS and $TiO_2/CdS/MoS_2$ photoanodes show photon conversion in the visible region. It is noteworthy that IPCE spectra are in consistent with the respective absorbance spectra (Fig. 4(d)). The current density obtained from integrating the IPCE and the spectral radiance, found to follow the same trend as that of LSV. Improved photon conversion arises from the formation of type II heterojunction between TiO_2 and CdS. Further improvement in $TiO_2/CdS/MoS_2$ compared to TiO_2/CdS, appears that the charge transfer property has been improved considerably due the presence of MoS_2. UV visible absorbance spectra for TiO_2, TiO_2/CdS and $TiO_2/CdS/MoS_2$ are presented in Fig. 4(d). TiO_2 NRs exhibit the absorption edge at 410 nm which corresponds to the band gap of rutile TiO_2 i.e. 3.2 eV. It is clearly seen that the absorption edge of the TiO_2 has been extended to the visible region after the decoration of CdS which is obviously due to the light sensitization from the narrow band gap of CdS. The absorbance spectra of $TiO_2/CdS/MoS_2$ shows similar absorbance behaviour to TiO_2/CdS implying that there is no band structure presence of MoS_2. The longer wavelength absorption after the band edges of TiO_2 and TiO_2/CdS emerged from the FTO background. The light absorption edge of the photoanode changed after it was heterojunctioned with CdS and MoS_2. The optical band gaps of bare TiO_2, TiO_2/CdS and $TiO_2/CdS/MoS_2$ heterojunction photoelectrodes have been calculated from Tauc plot and found to be 3.08 eV, 2.89 eV, and 2.91 eV, respectively (Fig. S10). These values confirm that the CdS a light sensitizer has extended the visible light absorption capacity of TiO_2 in TiO_2/CdS. However, MoS_2 has not significantly changed the optical band gap of TiO_2/CdS in $TiO_2/CdS/MoS_2$.

Electrochemical impedance spectroscopic (EIS) measurements have been carried out to further understand the charge transfer property of $TiO_2/CdS/MoS_2$ photoelectrode. EIS spectra were collected under 1 Sun illumination at 0.9 V vs RHE. Nyquist plot fitted with the equivalent circuit is shown in Figs. 5(a) and S11. The parameters extracted from the Nyquist plot are listed in the Table S1. Here, R_s is the series resistance R_{ct} is the charge transfer resistance across the electrode/electrolyte interface which is crucial to evaluate the semiconductor electrolyte charge process and C is the capacitance. The R_{ct} values obtained from the fitted Nyquist plot for TiO_2, TiO_2/CdS, and $TiO_2/CdS/MoS_2$ are 695, 668.8, and 120.10 Ω respectively. Generally, the larger value of R_{ct} indicates the slow charge transfer process across the interface. Parameters in Table S1 suggest that the R_{ct} decreases from pristine TiO_2 to TiO_2/CdS and it further decreases in $TiO_2/CdS/MoS_2$. It is evident that the photogenerated carrier transfer becomes faster in $TiO_2/CdS/MoS_2$ photoanode presumably due to the formation of type II heterojunction between TiO_2/CdS and hole scavenging by MoS_2.

To further understand the enhancement in the PEC activity, Mott-Schottky analysis have been carried for TiO_2, TiO_2/CdS, and $TiO_2/CdS/MoS_2$. Mott-Schottky measurements help to experimentally

demonstrate the type II heterojunction formation between TiO_2/CdS and $TiO_2/CdS/MoS_2$. Flat band potentials have been determined by X-intercept of the linear region. Flat band potential of the photoanode changed as it was heterojunctioned with CdS and MoS_2. The bare TiO_2, TiO_2/CdS and $TiO_2/CdS/MoS_2$ found to be -0.07, -0.11 and -0.22 V vs. RHE, respectively. These results are in consistent with the previous report [51]. The decrease in the slope of the curve indicates that the improvement in the carrier concentration of the photoanode. The negative shift in the flat band potential for TiO_2 in $TiO_2/CdS/MoS_2$ proves that the recombination of the photogenerated carriers have been reduced considerably. It is well known from the reports that 2 H MoS_2 can exhibit n or p type behaviour depending on the synthesis technique. Mott-Schottky plots show the positive slope for $TiO_2/CdS/MoS_2$ suggesting that the MoS_2 must be n-type material [52,53]. Hydrogen evolution was measured at 0 V vs. Ag/AgCl (0.9 V vs. RHE) using three electrode configuration. The hydrogen evolution as a function of time is shown in the Fig. 5d. The overall Faradaic efficiency is found to be around 96%.

Time resolved-photoluminescence (TR-PL) spectra provide profound knowledge on recombination process of the photoelectrode. To understand the contribution of MoS_2 in $TiO_2/CdS/MoS_2$ TR-PL spectra have been recorded at 337 nm excitation wavelength and presented in Fig. 6. The charge carrier kinetics and injection of the electron from CdS to TiO_2 can be revealed from TR-PL. There is a significant decrease in the lifetime from 5.06 ns to 4.03 ns when TiO_2 is heterojunctioned with CdS (Table 1). Higher electron transfer rate in TiO_2/CdS can be attributed to the type II band alignment of TiO_2 and CdS. Further decrease in the lifetime of charge carriers has been observed for $TiO_2/CdS/MoS_2$ compared to TiO_2/CdS heterojunction.

The longer lifetime of TiO_2/CdS (4.03 ns) in contrast to $TiO_2/CdS/MoS_2$ (3.04 ns) indicates that the electron transfer rate from CdS to TiO_2 is faster in the case of $TiO_2/CdS/MoS_2$. When electrons are photoexcited they can be injected into TiO_2 from CdS in $TiO_2/CdS/MoS_2$ faster than that of TiO_2/CdS. It is mainly due to the valance band edge of MoS_2 which is higher than that of CdS facilitates efficient transfer of holes from CdS valance band edge to that of MoS_2 resulting in reduced recombination loss. Based on the above results and the previous reports the energy band diagram has been proposed and displayed in Fig. 7 [54,55]. The enhancement in PEC activity of $TiO_2/CdS/MoS_2$ can be explained by the proposed mechanism below (Fig. 7). It has been shown that both n-type semiconductors TiO_2 and CdS form type II band alignment where holes transfer to the CBM of CdS while electrons migrate to the VBM of TiO_2. This behaviour agrees well with the Mott-Schottky results where flat band potential of TiO_2/CdS decreased compared to pristine TiO_2 (Table S2). In addition, the carrier lifetime of TiO_2/CdS (Table 1) has also been reduced indicating thermodynamically favorable condition has been achieved leading to considerable charge separation and hence enhanced photocurrent.

Previous results have shown MoS_2 as a good material for hydrogen evolution reaction (HER) as it possesses more negative potential for conduction band minimum which lies well above the hydrogen reduction potential [56,57]. Recent computational reports claim that the valance band of the monolayer MoS_2 is more positive than the water oxidation potential while the bulk MoS_2 is unsuitable for the overall water splitting [52,58]. S 2p orbital in MoS_2 makes this material a potential photoanode candidate in contrast with the metal oxides as the valance band edge for MoS_2 lies closer to the water oxidation potential. In case of CdS/MoS_2 system, MoS_2 is found to play versatile role in enhancing the photocatalytic activity depending on its n-type or p-type behaviour [23,25]. For instance, Li et al.'s work proved the loading of MoS_2 on CdS shows the junction formation between CdS and MoS_2 which was responsible for enhancement in photocatalytic activity. Therefore, authors considered that MoS_2 acts similar to noble metal and hence it plays a role of cocatalyst in CdS/MoS_2 system. The p-type MoS_2 forms p-n junction with the n-type CdS which also lead to improved photocurrent in CdS/MoS_2 heterojunction [23]. Zhu et al. reported type
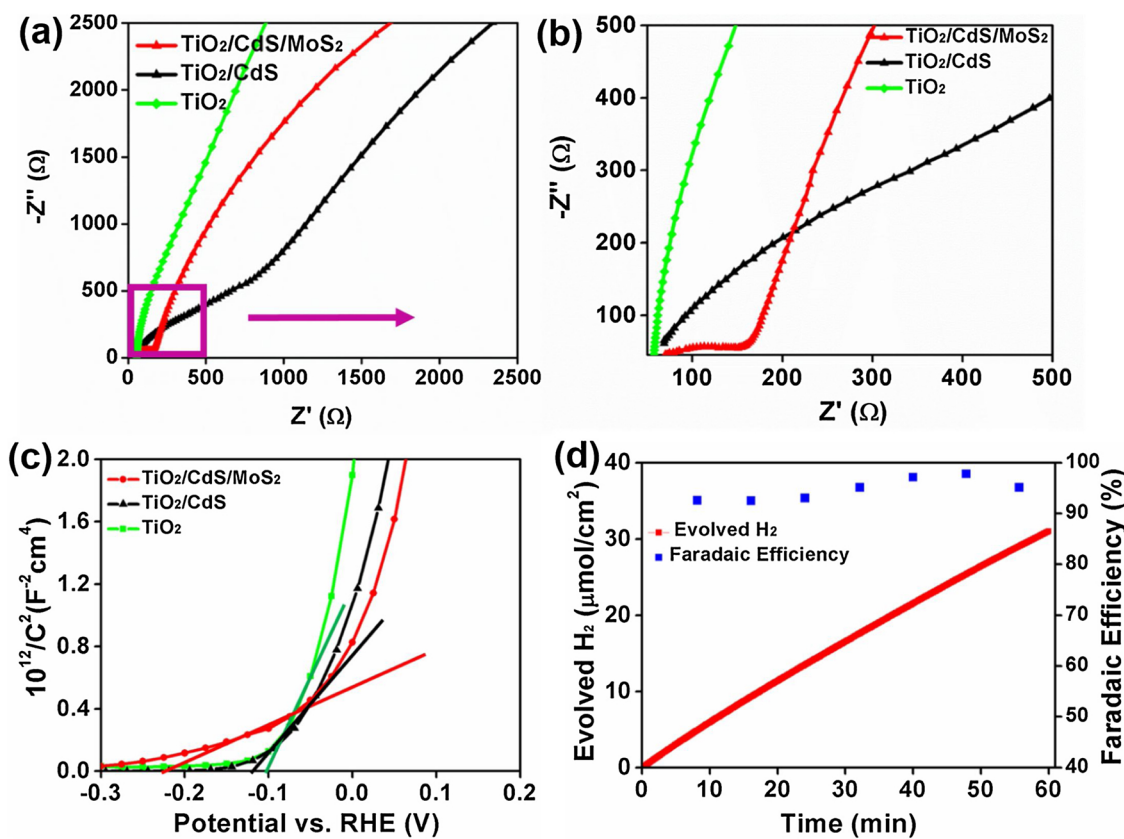
Fig. 5. (a) Electrochemical impedance spectra (EIS) of TiO$_2$/CdS/MoS$_2$, TiO$_2$/CdS and TiO$_2$. (b) Zoomed region of EIS spectra of (a). (c) Mott-Schottky for TiO$_2$/CdS/MoS$_2$, TiO$_2$/CdS and TiO$_2$. (d) Hydrogen evolution and Faradaic efficiency measurement at 0 V vs Ag/AgCl (0.9 V vs. RHE). All the above measurements were carried out in the aqueous solution of Na$_2$S and Na$_2$SO$_3$ electrolyte.
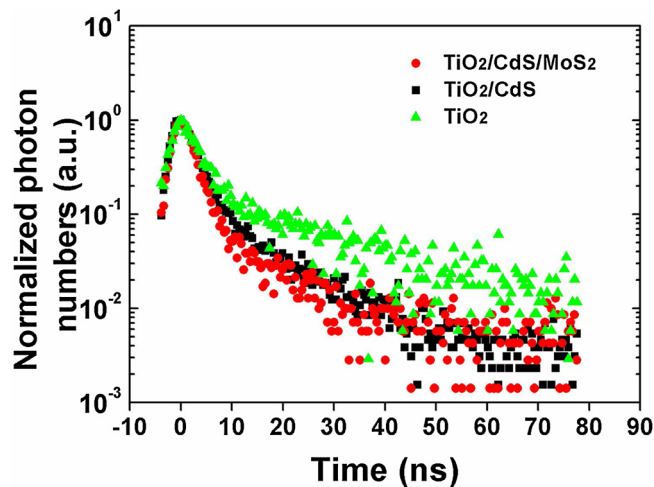

Fig. 6. TR-PL for TiO$_2$/CdS/MoS$_2$, TiO$_2$/CdS, and TiO$_2$.

Table 1
PL lifetime of TiO$_2$, TiO$_2$/CdS and TiO$_2$/CdS/MoS$_2$.

Samples	TiO$_2$	TiO$_2$/CdS	TiO$_2$/CdS/MoS$_2$
Lifetime (τ)	5.06 ns	4.03 ns	3.04 ns

I heterojunction which accounts for the enhanced carrier separation efficiency [57]. Whereas in case of TiO$_2$/MoS$_2$ photoanode, though CBM of MoS$_2$ lies below that of TiO$_2$, 2H-MoS$_2$ acts as a hole carrier and enhances the PEC property. In TiO$_2$/CdS/MoS$_2$ system, as shown by HRTEM the intimate contact formed between MoS$_2$ and CdS. The

valance band maximum of MoS$_2$ sheets is higher than that of the CdS, therefore, the holes generated upon photoexcitation in CdS can easily be transferred to MoS$_2$ whereas the photogenerated electrons on CBM of CdS migrate to TiO$_2$.

Qin et al. have investigated MoS$_2$/CdS-TiO$_2$ nanofiber photocatalysts in the powder form for H$_2$ evolution [59]. The morphology of the TiO$_2$-CdS photocatalyst is nanofiber while our current work presents the study of TiO$_2$ nanorod and CdS nanocrystal which are known to be very beneficial for the electron-hole pair migration [60]. Raja et al. have studied Pt free photoelectrode TiO$_2$/CdS with 1 T phase of the MoS$_2$ as co-catalyst [61]. The nanocrystalline powder of TiO$_2$ was used to fabricate the heterojunction. However, in our study MoS$_2$ forms a type I heterojunction with CdS and improves the photocurrent response.

We have compared different heterojunction photoanodes of TiO$_2$ with light sensitizing materials such as CdSe and CdS with different morphology as listed in Table 2. It is found that TiO$_2$/CdS/MoS$_2$ heterojunction photoanode exhibits enhanced performance compared to those listed in the Table 2 [62–64,54,65]. As the photocurrent density of all the photoanodes in our study reach the saturation at 0.5 V vs RHE, we have compared other photoelectrodes performances at 0.5 V vs RHE.

On the basis of the aforementioned experimental evidences, it is confirmed that the MoS$_2$ plays a crucial role in enhancing the photoresponse of TiO$_2$/CdS. Based on the photoesponse as shown in the LSV curves (Fig.4(a)), TiO$_2$/CdS/MoS$_2$ photoelectrode shows enhanced PEC performance due to the presence of MoS$_2$ NSs. It is reported that the MoS$_2$ and CdS form a type I heterojunction while TiO$_2$ and CdS form a type II heterojunction as shown in the schematic band diagram Fig. 7 [48,57]. The intimate contact established betweeen TiO$_2$/CdS and CdS/MoS$_2$, as depicted by HRTEM and XPS, facilitates the smooth diffusion
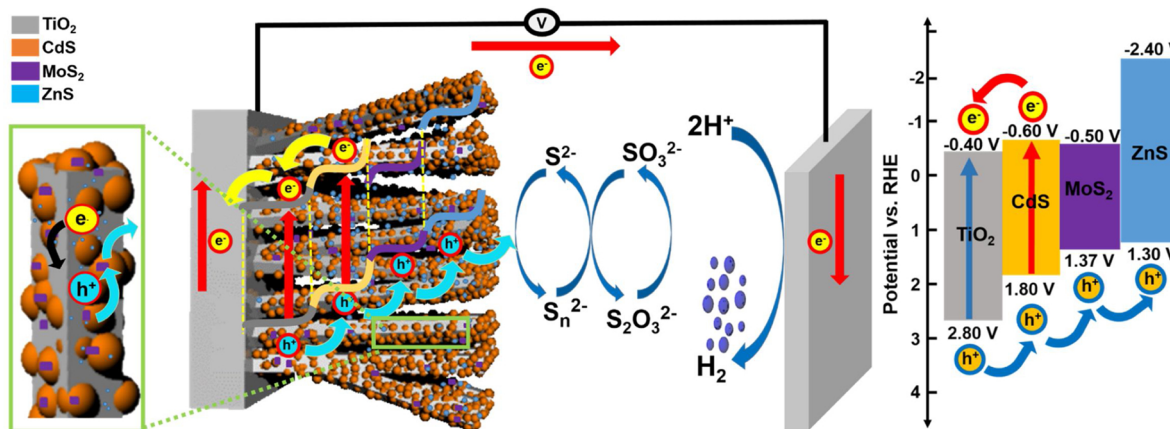
Fig. 7. Schematic diagram illustrating the charge transport mechanism in TiO$_2$/CdS/MoS$_2$ photoanode.

Table 2

The PEC performance of different TiO$_2$/chalcogenide based systems in the presence of Na$_2$S and Na$_2$SO$_3$ electrolyte at 0.5 V *vs.* RHE under one sun illumination.

Photoanodes	Morphology	Photocurrent density (mA/cm^2) at 0.5 V vs. RHE	Synthesis technique for TiO$_2$/Chalcogenide	Reference
TiO$_2$/CdS/MoS$_2$	Nanorod/nanocrystal/nanosheets	3.25	Hydrothermal/Chemical bath deposition	This work
TiO$_2$/CdSe/MoS$_2$	Porous TiO$_2$/CdSe nanoparticle	2.00	Sol-gel/Hydrothermal	[59]
TiO$_2$/CdS	TiO$_2$ nanoflower/CdS quantum dot	2.50	Hydrothermal/SILAR	[60]
TiO$_2$/CdS	TiO$_2$ nanorods/CdS nanoflower	3.10	Hydrothermal/Hydrothermal	[61]
TiO$_2$/CdS/Co-Pi	TiO$_2$ nanowire/CdS quantum dot	1.00	Hydrothermal/Chemical vapor deposition	[51]
H:TiO$_2$/CdS/CdSe	TiO$_2$ nanobullet/CdS quantum dot	1.20	Hydrothermal/SILAR	[62]

of charge carriers. When electrons are photoexcited they can be injected into TiO$_2$ from CdS in TiO$_2$/CdS/MoS$_2$ faster than that of TiO$_2$/CdS. It is mainly due to the valance band edge of MoS$_2$, which is higher than that of CdS, facilitates efficient transfer of holes from CdS valance band edge to that of MoS$_2$ resulting in reduced recombination loss. This was further supported by PL lifetime measurement. The decrease in the lifetime of the charge carriers indicates that the reduced recombination rate in TiO$_2$/CdS/MoS$_2$. It clearly suggests that the role of MoS$_2$ in improving the separation of electron-hole pairs. EIS results also corroborate this observation as the charge transfer resistance decreases for TiO$_2$/CdS/MoS$_2$ compared to TiO$_2$/CdS. Considering all these facts, the tentative mechanism has been proposed as shown in the Fig. 7 depicting the role of MoS$_2$ in enhancing the PEC performance as MoS$_2$ semiconductor improves the charge separation by forming type I heterojunction with CdS. Subsequently, the holes are transported to valance band of ZnS and to the electrolyte for further oxidation.

To the best of our knowledge, this is the first report of TiO$_2$/CdS/MoS$_2$ where MoS$_2$ NSs contributed for the enhanced PEC performance in TiO$_2$/CdS heterojunctions. MoS$_2$ NSs facilitate thermodynamically favourable condition which reduces the recombination rate and the transfer of electrons from CdS to TiO$_2$ which obviously induces high photoactivity.

5. Conclusion

Heterojunction of TiO$_2$/CdS/MoS$_2$ photoanode has been fabricated by all solution method and found to show promising PEC activity. TiO$_2$/CdS/MoS$_2$ photoelectrode shows the photocurrent density much higher than pristine TiO$_2$ and TiO$_2$/CdS heterojunction. The influence of MoS$_2$ NSs on TiO$_2$/CdS/MoS$_2$ heterojunction was systematically investigated. The enhanced PEC performance was attributed to the increased charge transfer efficiency which resulted from the intimate contact between the individual materials in TiO$_2$/CdS/MoS$_2$ heterojunction. TiO$_2$/CdS/MoS$_2$ shows the extended lifetime of the photogenerated carriers against the recombination compared to that of TiO$_2$ and TiO$_2$/CdS. The staggered band alignment in TiO$_2$/CdS and hole capturing ability of MoS$_2$ NSs created a facile thermodynamic condition to improve

photoelectrochemical performance. This results show that the simple fabrication of promising heterojunction photoanode comprising of three different materials from all solution process. This work also proves that MoS$_2$ NSs can successfully be utilized in photoanodes where it acts as a good hole capturing material. It would pave the way to design and fabricate future energy materials to achieve sustainable energy system.

Acknowledgements

Appendix A. Supplementary data

Supplementary material related to this article can be found, in the online version, at doi:https://doi.org/10.1016/j.apcatb.2019.118102.

References

[1] K. Zhang, M. Ma, P. Li, D.H. Wang, J.H. Park, Water splitting progress in tandem devices: moving photolysis beyond electrolysis, Adv. Energy Mater. 6 (2016) 1–16, https://doi.org/10.1002/aenm.201600602.

[2] C. Jiang, S.J.A. Moniz, A. Wang, T. Zhang, J. Tang, Photoelectrochemical devices for solar water splitting-materials and challenges, Chem. Soc. Rev. 46 (2017) 4645–4660, https://doi.org/10.1039/c6cs00306k.

[3] J. Jia, L.C. Seitz, J.D. Benck, Y. Huo, Y. Chen, J.W.D. Ng, T. Bilir, J.S. Harris, T.F. Jaramillo, Solar water splitting by photovoltaic-electrolysis with a solar-to-hydrogen efficiency over 30%, Nat. Commun. 7 (2016) 1–6, https://doi.org/10.1038/ncomms13237.

[4] L. Hao, L. Kang, H. Huang, L. Ye, K. Han, S. Yang, H. Yu, M. Batmunkh, Y. Zhang, T. Ma, Surface-halogenation-Induced atomic-site activation and local charge separation for superb CO2 photoreduction, Adv. Mater. 31 (2019) 1–7, https://doi.org/10.1002/adma.201900546.

[5] F. Chen, H. Huang, L. Guo, Y. Zhang, T. Ma, The role of polarization in photocatalysis, Angew. Chem. Int. Ed. (2019) 10061–10073, https://doi.org/10.1002/

anie.201901361.

[6] D.R. Tobergte, S. Curtis, Application of Titanium Dioxide Photocatalysis to Construction Materials, (2013), https://doi.org/10.1017/CBO9781107415324.004.

[7] S.J.A. Moniz, S.A. Shevlin, D.J. Martin, Z.-X. Guo, J. Tang, Visible-light driven heterojunction photocatalysts for water splitting—a critical review, Energy Environ. Sci. 8 (2015) 731–759, https://doi.org/10.1039/C4EE03271C.

[8] A.P. Singh, N. Kodan, B.R. Mehta, A. Held, L. Mayrhofer, M. Moseler, Band edge engineering in BiVO4/TiO2 heterostructure: enhanced photoelectrochemical performance through improved charge transfer, ACS Catal. 6 (2016) 5311–5318, https://doi.org/10.1021/acscatal.6b00956.

[9] S.S. Kment, P. Schmuki, R. Zboril, S. Kment, F. Riboni, S. Pausova, L. Wang, L. Wang, Photoanodes based on TiO2 and a-Fe2O3 for solar water splitting – superior role of 1D nanoarchitectures and of combined heterostructures, Chem. Soc. Rev. 46 (2017) 3716–3769, https://doi.org/10.1039/C6CS00015K.

[10] M. Ge, Q. Li, C. Cao, J. Huang, S. Li, S. Zhang, Z. Chen, K. Zhang, S.S. Al-Deyab, Y. Lai, One-dimensional TiO2 nanotube photocatalysts for solar water splitting, Adv. Sci. 4 (2017) 1600152, https://doi.org/10.1002/advs.201600152.

[11] Y. He, N.B. Sutton, H.H.H. Rijnaarts, A.A.M. Langenhoff, Degradation of pharmaceuticals in wastewater using immobilized TiO2 photocatalysis under simulated solar irradiation, Appl. Catal. B: Environ. 182 (2016) 132–141, https://doi.org/10.1016/j.apcatb.2015.09.015.

[12] X. Gao, X. Liu, Z. Zhu, Y. Gao, Q. Wang, F. Zhu, Z. Xie, Enhanced visible light photocatalytic performance of CdS sensitized TiO2 nanorod arrays decorated with Au nanoparticles as electron sinks, Sci. Rep. 7 (2017) 973, https://doi.org/10.1038/s41598-017-01124-5.

[13] Y.S. Chang, M. Choi, M. Baek, P.Y. Hsieh, K. Yong, Y.J. Hsu, CdS/CdSe co-sensitized brookite H:TiO2 nanostructures: charge carrier dynamics and photoelectrochemical hydrogen generation, Appl. Catal. B: Environ. 225 (2018) 379–385, https://doi.org/10.1016/j.apcatb.2017.11.063.

[14] W. Zhou, Z. Yin, Y. Du, X. Huang, Z. Zeng, Z. Fan, H. Liu, J. Wang, H. Zhang, Synthesis of few-layer MoS2 nanosheet-coated TiO2 nanobelt heterostructures for enhanced photocatalytic activities, Small 9 (2013) 140–147, https://doi.org/10.1002/smll.201201161.

[15] J. Chen, X.J. Wu, L. Yin, B. Li, X. Hong, Z. Fan, B. Chen, C. Xue, H. Zhang, One-pot synthesis of CdS nanocrystals hybridized with single-layer transition-metal dichalcogenide nanosheets for efficient photocatalytic hydrogen evolution, Angew. Chem. Int. Ed. 54 (2015) 1210–1214, https://doi.org/10.1002/anie.201410712.

[16] X.J. Wu, J. Chen, C. Tan, Y. Zhu, Y. Han, H. Zhang, Controlled growth of high-density CdS and CdSe nanorod arrays on selective facets of two-dimensional semiconductor nanoplates, Nat. Chem. 8 (2016) 470–475, https://doi.org/10.1038/nchem.2473.

[17] X. Chen, W. Shangguan, Hydrogen production from water splitting on CdS-based photocatalysts using solar light, Front. Energy 7 (2013) 111–118, https://doi.org/10.1007/s11708-012-0228-4.

[18] Y. Tang, X. Hu, C. Liu, Perfect inhibition of CdS photocorrosion by graphene sheltering engineering on TiO2 nanotube array for highly stable photocatalytic activity, Phys. Chem. Chem. Phys. 16 (2014) 25321–25329, https://doi.org/10.1039/c4cp04057k.

[19] X. Gao, X. Liu, Z. Zhu, Y. Gao, Q. Wang, F. Zhu, Z. Xie, Enhanced visible light photocatalytic performance of CdS sensitized TiO2 nanorod arrays decorated with Au nanoparticles as electron sinks, Sci. Rep. 7 (2017) 973, https://doi.org/10.1038/s41598-017-01124-5.

[20] C.H. Chang, Y.L. Lee, Chemical bath deposition of CdS quantum dots onto mesoscopic TiO2 films for application in quantum-dot-sensitized solar cells, Appl. Phys. Lett. 91 (2007) 053503, https://doi.org/10.1063/1.2768311.

[21] R. Nakamura, S. Makuta, Y. Tachibana, Electron injection dynamics at the SILAR deposited CdS quantum dot/TiO2 interface, J. Phys. Chem. C 119 (2015) 20357–20362, https://doi.org/10.1021/acs.jpcc.5b06900.

[22] X. Xu, G. Zhou, X. Dong, J. Hu, Interface band engineering charge transfer for 3D MoS2 photoanode to boost photoelectrochemical water splitting, ACS Sustain. Chem. Eng. 5 (2017) 3829–3836, https://doi.org/10.1021/acssuschemeng.6b02883.

[23] Y. Liu, Y.X. Yu, W. De Zhang, MoS2/CdS heterojunction with high photoelectrochemical activity for H2 evolution under visible light: the role of MoS2, J. Phys. Chem. C 117 (2013) 12949–12957, https://doi.org/10.1021/jp4009652.

[24] F.M. Pesci, M.S. Sokolikova, C. Grotta, P.C. Sherrell, F. Reale, K. Sharda, N. Ni, P. Palczynski, C. Mattevi, MoS2/WS2 heterojunction for photoelectrochemical water oxidation, ACS Catal. (2017) 4990–4998, https://doi.org/10.1021/acscatal.7b01517.

[25] X. Zong, G. Wu, H. Yan, G. Ma, J. Shi, F. Wen, L. Wang, C. Li, Photocatalytic H2 evolution on MoS2/CdS catalysts under visible light irradiation, J. Phys. Chem. C 114 (2010) 1963–1968, https://doi.org/10.1021/Jp904350e.

[26] Y. Yang, Y. Zhang, Z. Fang, L. Zhang, Z. Zheng, Z. Wang, W. Feng, S. Weng, S. Zhang, P. Liu, Simultaneous realization of enhanced photoactivity and promoted photostability by multilayered MoS2 coating on CdS nanowire structure via compact coating methodology, ACS Appl. Mater. Interfaces 9 (2017) 6950–6958, https://doi.org/10.1021/acsami.6b09873.

[27] Y.P. Xie, Z.B. Yu, G. Liu, X.L. Ma, H.M. Cheng, CdS-mesoporous ZnS core-shell particles for efficient and stable photocatalytic hydrogen evolution under visible light, Energy Environ. Sci. 7 (2014) 1895–1901, https://doi.org/10.1039/c3ee43750g.

[28] B. Liu, E.S. Aydil, Growth of oriented single-crystalline rutile TiO2 nanorods on transparent conducting substrates for dye-sensitized solar cells, J. Am. Chem. Soc. (2009), https://doi.org/10.1021/ja8078972.

[29] S. Cheng, W. Fu, H. Yang, L. Zhang, J. Ma, H. Zhao, M. Sun, L. Yang,

[30] C. Li, H. Zhang, C. Cheng, CdS/CdSe co-sensitized 3D SnO2/TiO2 sea urchin-like nanotube arrays as an efficient photoanode for photoelectrochemical hydrogen generation, RSC Adv. 6 (2016) 37407–37411, https://doi.org/10.1039/C6RA02176J.

[31] C. Cheng, S.K. Karuturi, L. Liu, J. Liu, H. Li, L.T. Su, A.I.Y. Tok, H.J. Fan, Quantum-dot-Sensitized TiO2 inverse opals for photoelectrochemical hydrogen generation, Small 8 (2012) 37–42, https://doi.org/10.1002/smll.201101660.

[32] L.C. Kao, S.Y.H. Liou, C.L. Dong, P.H. Yeh, C.L. Chen, Tandem structure of QD cosensitized TiO2 nanorod arrays for solar light driven hydrogen generation, ACS Sustain. Chem. Eng. 4 (2016) 210–218, https://doi.org/10.1021/acssuschemeng.5b01010.

[33] Q. Geng, X. Tong, G. Evans Wenya, C. Yang, J. Wang, A.S. Maloletnev, Z.M. Wang, X. Su, Humate-assisted synthesis of MoS2/C nanocomposites via Co-precipitation/calcination route for high performance lithium ion batteries, Nanoscale Res. Lett. 13 (2018) 129–137, https://doi.org/10.1186/s11671-018-2537-y.

[34] R.K. Kokal, P. Naresh Kumar, M. Deepa, A.K. Srivastava, Lead selenide quantum dots and carbon dots amplify solar conversion capability of a TiO2/CdS photoanode, J. Mater. Chem. A 3 (2015) 20715–20726, https://doi.org/10.1039/C5TA04393J.

[35] S.A. Pawar, R.S. Devan, D.S. Patil, V.V. Burungale, T.S. Bhat, S.S. Mali, S.W. Shin, J.E. Ae, C.K. Hong, Y.R. Ma, J.H. Kim, P.S. Patil, Hydrothermal growth of photoelectrochemically active titanium dioxide cauliflower-like nanostructures, Electrochim. Acta 117 (2014), https://doi.org/10.1016/j.electacta.2013.11.182.

[36] B. Sun, T. Shi, X. Tan, Z. Liu, Y. Wu, G. Liao, Iridium oxide modified CdSe/CdS/TiO2 nanorods for efficient and stable photoelectrochemical water splitting, Mater. Today Proc. 3 (2016) 443–448, https://doi.org/10.1016/J.MATPR.2016.01.040.

[37] M. Samadpour, P.P. Boix, S. Giménez, A. Iraji Zad, N. Taghavinia, I. Mora-Seró, J. Bisquert, Fluorine treatment of TiO2 for enhancing quantum dot sensitized solar cell performance, J. Phys. Chem. C 115 (2011) 14400–14407, https://doi.org/10.1021/jp202819y.

[38] D.S. Patil, S.A. Pawar, J.C. Shin, Core-shell structure of Co3O4@CdS for high performance electrochemical supercapacitor, Chem. Eng. J. 335 (2018) 693–702, https://doi.org/10.1016/J.CEJ.2017.11.007.

[39] Z. Lian, P. Xu, W. Wang, D. Zhang, S. Xiao, X. Li, G. Li, C60-decorated CdS/TiO2 mesoporous architectures with enhanced photostability and photocatalytic activity for H2 evolution, ACS Appl. Mater. Interfaces 7 (2015) 4533–4540, https://doi.org/10.1021/am5088665.

[40] Z. Chen, Y.-J. Xu, Ultrathin TiO2 layer Coated-CdS spheres core–Shell nanocomposite with enhanced visible-light photoactivity, ACS Appl. Mater. Interfaces 5 (2013) 13353–13363, https://doi.org/10.1021/am4043068.

[41] T. Lin, J. Wang, L. Guo, F. Fu, Fe3O4@MoS2 core–shell composites: preparation, characterization, and catalytic application, J. Phys. Chem. C 119 (2015) 13658–13664, https://doi.org/10.1021/acs.jpcc.5b02516.

[42] J. Xie, J. Zhang, S. Li, F. Grote, X. Zhang, H. Zhang, R. Wang, Y. Lei, B. Pan, Y. Xie, Controllable disorder engineering in oxygen-incorporated MoS2 ultrathin nanosheets for efficient hydrogen evolution, J. Am. Chem. Soc. 135 (2013) 17881–17888, https://doi.org/10.1021/ja408329q.

[43] C. Zhao, X. Wang, J. Kong, J.M. Ang, P.S. Lee, Z. Liu, X. Lu, Self-assembly-Induced alternately stacked single-layer MoS2 and N-doped graphene: a novel van der waals heterostructure for lithium-ion batteries, ACS Appl. Mater. Interfaces 8 (2016) 2372–2379, https://doi.org/10.1021/acsami.5b11492.

[44] X. Zhao, X. Ku, K. Yan, H. Wang, Z. Wang, S. Yang, Space-confined growth of MoS2 nanosheets within graphite: the layered hybrid of MoS2 and graphene as an active catalyst for hydrogen evolution reaction, Chem. Mater. 26 (2014) 2344–2353, https://doi.org/10.1021/cm500347r.

[45] N.P. Kondekar, M.G. Boebinger, E.V. Woods, M.T. McDowell, In situ XPS investigation of transformations at crystallographically oriented MoS2 interfaces, ACS Appl. Mater. Interfaces 9 (2017) 32394–32404, https://doi.org/10.1021/acsami.7b10230.

[46] R.S. Devan, V.P. Thakare, V.V. Antad, P.R. Chikate, R.T. Khare, M.A. More, R.S. Dhayal, S.I. Patil, Y.-R. Ma, L. Schmidt-Mende, Nano-heteroarchitectures of two-dimensional MoS2@ one-dimensional brookite TiO2 nanorods: prominent electron emitters for displays, ACS Omega 2 (2017) 2925–2934, https://doi.org/10.1021/acsomega.7b00345.

[47] S. Gauthier, B. Reisberg, M. Zaudig, R.C. Petersen, K. Ritchie, K. Broich, S. Belleville, H. Brodaty, D. Bennett, H. Chertkow, J.L. Cummings, M. de Leon, H. Feldman, M. Ganguli, H. Hampel, P. Scheltens, M.C. Tierney, P. Whitehouse, B. Winblad, Photoelectrochemical cells, Lancet 367 (2001) 1262–1270, https://doi.org/10.1016/S0140-6736(06)68542-5.

[48] L. Liu, H. Hou, L. Wang, R. Xu, Y. Lei, S. Shen, D. Yang, W. Yang, A transparent CdS@TiO2 nanotextile photoanode with boosted photoelectrocatalytic efficiency and stability, Nanoscale 9 (2017) 15650–15657, https://doi.org/10.1039/c7nr05658c.

[49] B. Liu, Y. Xue, J. Zhang, D. Wang, T. Xie, X. Suo, L. Mu, H. Shi, Study on photoinduced charge transfer in the heterointerfaces of CuInS2/CdS co-sensitized mesoporous TiO2 photoelectrode, Electrochim. Acta 192 (2016) 370–376, https://doi.org/10.1016/j.electacta.2016.01.224.

[50] F. Huang, Q. Zhang, B. Xu, J. Hou, Y. Wang, R.C. Massé, S. Peng, J. Liu, G. Cao, A comparison of ZnS and ZnSe passivation layers on CdS/CdSe co-sensitized quantum dot solar cells, J. Mater. Chem. A 4 (2016) 14773–14780, https://doi.org/10.1039/c6ta01590e.

[51] L. Sang, H. Tan, X. Zhang, Y. Wu, C. Ma, C. Burda, Effect of quantum dot deposition on the interfacial flatband potential, depletion layer in TiO2 nanotube electrodes, and resulting H2 generation rates, J. Phys. Chem. C 116 (2012) 18633–18640,

https://doi.org/10.1021/jp305388c.

[52] Y. Pi, Z. Li, D. Xu, J. Liu, Y. Li, F. Zhang, G. Zhang, W. Peng, X. Fan, 1T-phase MoS2Nanosheets on TiO2 nanorod arrays: 3D photoanode with extraordinary catalytic performance, ACS Sustain. Chem. Eng. 5 (2017) 5175–5182, https://doi.org/10.1021/acssuschemeng.7b00518.

[53] Z. Chen, A.J. Forman, T.F. Jaramillo, Bridging the gap between bulk and nanostructured photoelectrodes: the impact of surface states on the electrocatalytic and photoelectrochemical properties of MoS2, J. Phys. Chem. C 117 (2013) 9713–9722, https://doi.org/10.1021/jp311375k.

[54] G. Ai, H. Li, S. Liu, R. Mo, J. Zhong, Solar water splitting by TiO2/CdS/Co – Pi nanowire array photoanode enhanced with Co – Pi as hole transfer relay and CdS as light absorber, Adv. Funct. Mater. 25 (2015) 5706–5713, https://doi.org/10.1002/adfm.201502461.

[55] J. Li, M.W.G. Hoffmann, H. Shen, C. Fabrega, J.D. Prades, T. Andreu, F. Hernandez-Ramirez, S. Mathur, Enhanced photoelectrochemical activity of an excitonic staircase in CdS@TiO2 and CdS@anatase@rutile TiO2 heterostructures, J. Mater. Chem. 22 (2012) 20472–20476, https://doi.org/10.1039/c2jm33404f.

[56] Q. Wang, J. Huang, H. Sun, Y.H. Ng, K.-Q. Zhang, Y. Lai, MoS$_2$ quantum Dots@TiO$_2$ nanotube arrays: an extended-spectrum-driven photocatalyst for solar hydrogen evolution, ChemSusChem 11 (2018) 1708–1721, https://doi.org/10.1002/cssc.201800379.

[57] X. Zhu, P. Wang, Q. Zhang, Z. Wang, Y. Liu, X. Qin, X. Zhang, Y. Dai, B. Huang, CdS-MoS2 heterostructures on Mo substrates via in situ sulfurization for efficient photoelectrochemical hydrogen generation, RSC Adv. 7 (2017) 44626–44631, https://doi.org/10.1039/c7ra06304k.

[58] W.N. Zhao, Z.P. Liu, Mechanism and active site of photocatalytic water splitting on titania in aqueous surroundings, J. Am. Chem. Soc. 132 (2010) 13008–13015, https://doi.org/10.1039/c3sc53385a.

[59] N. Qin, J. Xiong, R. Liang, Y. Liu, S. Zhang, Y. Li, Z. Li, L. Wu, Highly efficient photocatalytic H2 evolution over MoS2/CdS-TiO2 nanofibers prepared by an electrospinning mediated photodeposition method, Appl. Catal. B: Environ. 202 (2017) 374–380, https://doi.org/10.1016/j.apcatb.2016.09.040.

[60] Z. Xie, X. Liu, W. Wang, C. Liu, Z. Li, Z. Zhang, Enhanced photoelectrochemical properties of TiO2 nanorod arrays decorated with CdS nanoparticles, Sci. Technol. Adv. Mater. 15 (2014), https://doi.org/10.1088/1468-6996/15/5/055006.

[61] R. Raja, P. Sudhagar, A. Devadoss, C. Terashima, L.K. Shrestha, K. Nakata, R. Jayavel, K. Ariga, A. Fujishima, Pt-free solar driven photoelectrochemical hydrogen fuel generation using 1T MoS2 co-catalyst assembled CdS QDs/TiO2 photoelectrode, Chem. Commun. 51 (2015) 522–525, https://doi.org/10.1039/c4cc07304e.

[62] Y. Wang, F. Zhang, M. Yang, Z. Wang, Y. Ren, J. Cui, Y. Zhao, J. Du, K. Li, W. Wang, D.J. Kang, Synthesis of porous MoS2/CdSe/TiO2 photoanodes for photoelectrochemical water splitting, Microporous Mesoporous Mater. 284 (2019) 403–409, https://doi.org/10.1016/j.micromeso.2019.04.055.

[63] H. Li, X. Wang, X. Li, J. Xi, Z. Ji, The promising photoanode of Pt coupled TiO2 NFs/CdS QDs with enhanced photoelectrochemical performance, J. Alloys Compd. 790 (2019) 900–908, https://doi.org/10.1016/j.jallcom.2019.03.261.

[64] S. David, M.A. Mahadik, H.S. Chung, J.H. Ryu, J.S. Jang, Facile hydrothermally synthesized a novel CdS nanoflower/rutile-TiO2 nanorod heterojunction photoanode used for photoelectrocatalytic hydrogen generation, ACS Sustain. Chem. Eng. 5 (2017) 7537–7548, https://doi.org/10.1021/acssuschemeng.7b00558.

[65] Y.S. Chang, M. Choi, M. Baek, P.Y. Hsieh, K. Yong, Y.J. Hsu, CdS/CdSe co-sensitized brookite H:TiO2 nanostructures: charge carrier dynamics and photoelectrochemical hydrogen generation, Appl. Catal. B: Environ. 225 (2018) 379–385, https://doi.org/10.1016/j.apcatb.2017.11.063.

Update

Applied Catalysis B: Environmental

Erratum to "Substantially enhanced photoelectrochemical performance of TiO$_2$ nanorods/CdS nanocrystals heterojunction photoanode decorated with MoS$_2$ nanosheets" [Appl. Catal. B 259 (2019) 118102]

Swetha S.M. Bhat[a,1], Sachin A. Pawar[b,1], Darshna Potphode[c], Chang-Ki Moon[a], Jun Min Suh[a], Changyeon Kim[a], Seokhoon Choi[a], Dipali S. Patil[b], Jang-Joo Kim[a], Jae Cheol Shin[b,*], Ho Won Jang[a,*]

[a] Department of Materials Science and Engineering, Research Institute of Advanced Materials, Seoul National University, Seoul, 08826, Republic of Korea
[b] Department of Physics, Yeungnam University, Gyeongsan, Gyeongbuk, 38541, Republic of Korea
[c] Department of Chemical Engineering, Indian Institute of Technology (IIT), Hyderabad, Kandi, Sangareddy, 502285, Telangana, India

The publisher regrets that the article has been published without proof-reading.

Please find the correct version of the graphical abstract, Fig. 7, Table 2 and acknowledgement. The publisher would like to apologise for any inconvenience caused.

Graphical Abstract
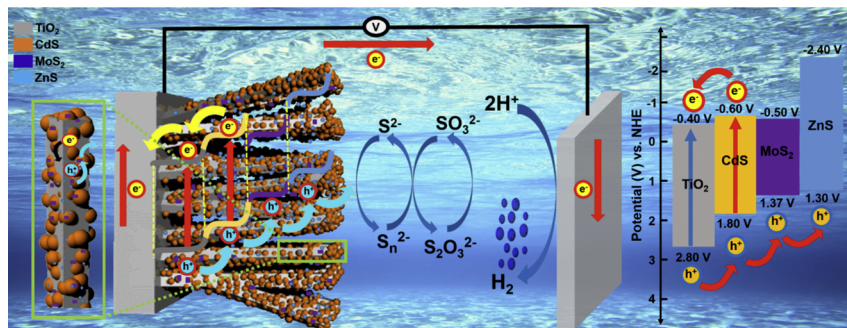
* Corresponding authors.
E-mail addresses: jcshin@yu.ac.kr (J.C. Shin), hwjang@snu.ac.kr (H.W. Jang).
[1] These authors contributed equally to this work.
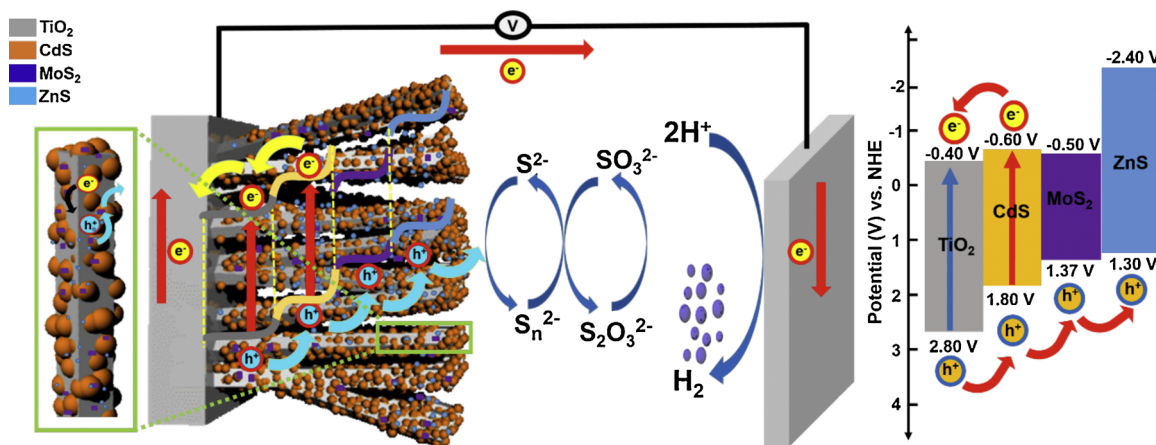
Fig. 7 Schematic diagram illustrating the charge transport mechanism in TiO_2/CdS/MoS_2 photoanode.

Table 2. The PEC performance of different TiO_2/chalcogenide based systems in the presence of Na_2S and Na_2SO_3 in electrolyte at 0.5 V *vs.* RHE under one sun illumination.

Photoanodes	Morphology	Photocurrent density (mA/cm²)	Synthesis technique for TiO_2/Chalcogenide	Reference
TiO_2/CdS/MoS_2	Nanorod/nanocrystal/ nanosheets	3.25	Hydrothermal/Chemical bath deposition	**This work**
TiO_2/CdSe/MoS_2	Porous TiO_2/CdSe nanoparticle	2.0	Sol-gel + Hydrothermal	[62]
TiO_2/CdS	TiO_2 nanoflower/CdS quantum dot	2.5	Hydrothermal/SILAR	[63]
TiO_2/CdS	TiO_2 nanorods/CdS nanoflower	3.1	Hydrothermal/Hydrothermal	[64]
TiO_2/CdS/Co-Pi	TiO_2 nanowire/CdS Quantum dot	1.0	Hydrothermal/Chemical vapor deposition	[54]
H:TiO_2/CdS/CdSe	TiO_2 nanobullet/CdS quantum dot	1.2	Hydrothermal/SILAR	[65]

Acknowledgements